Sporadic *E* morphology from GPS-CHAMP radio occultation

Dong L. Wu, Chi O. Ao, George A. Hajj, Manuel de la Torre Juarez, and Anthony J. Mannucci

Jet Propulsion Laboratory, California Institute of Technology, Pasadena, California, USA

Received 23 July 2004; revised 28 October 2004; accepted 19 November 2004; published 19 January 2005.

[1] The scintillations of phase and amplitude in terms of signal-to-noise ratio (SNR) of the GPS radio occultation signal are caused by thin ionization layers. These thin irregular electron density layers in the *E* region ionosphere are often called sporadic *E* (E_s). For a monthly retrieval of E_s morphology we use the variances of the phase and SNR fluctuations of worldwide ~6000 GPS/CHAMP occultations in the *E* region. The E_s climatology is studied globally with the SNR and phase variances in terms of monthly zonal means, seasonal maps, and diurnal and long-term variations. The zonal mean variances reveal strong, extended E_s activities at summertime midlatitudes but weak, confined activities in wintertime high latitudes, peaking at ~105 km. Global maps at 105-km altitude show clear dependence of E_s activities on the geomagnetic dip angle, where the summertime midlatitude E_s occurs mostly at dip angles of 30°–60° and the wintertime high-latitude enhancement occurs mostly at dip angles >80°. The midlatitude E_s variances exhibit a strong semidiurnal variation with peak hours near 0800–1000 and 2000 local solar time, respectively. The peak hours are delayed slightly with decreasing height, suggesting influences from the semidiurnal tide. To provide more insights on the observed SNR and phase variances, we model radio wave propagation for the CHAMP observing geometry under several perturbed cases in the *E* region ionosphere. The model simulations indicate that the SNR variance has the maximum response to E_s perturbations at vertical wavelengths of ~1.2 km, whereas the phase response maximizes at ~2 km (for the 1-s variance analysis). The characteristic scale depends little on the truncation time used in the SNR variance analysis, but it increases with the truncation time for the phase variances. Initial studies show that reasonable global E_s morphology can be produced on a monthly and seasonal basis with the CHAMP one-antenna occultations. Better results from other existing and upcoming GPS occultation missions are anticipated in future studies, and they will significantly improve our understanding of this important phenomenon.

Citation: Wu, D. L., C. O. Ao, G. A. Hajj, M. de la Torre Juarez, and A. J. Mannucci (2005), Sporadic *E* morphology from GPS-CHAMP radio occultation, *J. Geophys. Res.*, *110*, A01306, doi:10.1029/2004JA010701.

1. Introduction

[2] Sporadic *E* (E_s) is known as a transient phenomenon where high-density ion layers form in a narrow-altitude region in the *E* region ionosphere. Knowledge of global E_s properties and effects is of great interest to radio communications and navigations. Advances in solar terrestrial physics and atmospheric dynamics require a better understanding of the electric conductivity and its variability in the *E* region. Detailed physical and statistical descriptions of the E_s processes, especially from a global perspective, are essential for understanding their formation and variations and ultimately for improving numerical forecast of space weather.

[3] Observations of E_s in the past were mostly from ground-based remote sensing, sometimes in situ techniques, and only recently from satellite sensors [e.g., *Farley*, 1985; *Whitehead*, 1989; *Kelly*, 1989; *Mathews*, 1998; *Hocke et al.*, 2001, and references therein]. As reported from ionosonde and incoherent scatter radar data (i.e., electron density, electric field, etc.), E_s layers usually occur around 90–110 km altitudes with thickness of 0.5–5 km and a horizontal extent of 10–1000 km. The thin and patchy layers of enhanced electron density, sometimes also called E_s clouds, may last from minutes to hours causing radio signal interruption or frequency drift. Strong local time and seasonal variations of midlatitude E_s have been observed, showing the maximums in daytime hours and during summer months. E_s observations remain limited to a few geographical locations, and theories (including the well-known wind shear theory) still have difficulties quantitatively explaining E_s formation and variability in many situations.

[4] E_s variabilities exist over broad temporal and spatial scales, which are believed to be related to other atmospheric and ionospheric processes. For instance, radar

0148-0227/05/2004JA010701$09.00

observations show strong short-period field-aligned structures imbedded in long-period E_s irregularities, which are consistent with gravity wave characteristics in that region [*Tsunoda et al.*, 1994; *Fukao et al.*, 1998]. *Pancheva et al.* [2003] reported significant correlation between radar wind measurements and E_s variations near 100 km, which was attributed to planetary and tidal wave modulations. E_s occurrences are also influenced by solar activities [*Baggaley*, 1984; *Maksyutin et al.*, 2001] and convective systems in the troposphere [*Shrestha*, 1971; *Datta*, 1972]. *Hocke et al.* [2001] studied E_s irregularities using GPS/Meteorology (GPS/MET) phase measurements and found that strong activities occur mostly at heights between 95 and 105 km at summertime midlatitudes. These E_s irregularities appear to correlate with deep convective and topography-induced processes in the troposphere [*Hocke and Tsuda*, 2001; *Hocke et al.*, 2002]. In addition, linkage of E_s to other ionospheric phenomena, including spread *F* and traveling ionospheric disturbance, has also been investigated [*Tsunoda and Cosgrove*, 2001].

[5] Techniques for E_s observations have been advanced remarkably in recent years. Satellite-to-satellite radio communications, such as Global Positioning System-Low Earth Orbiter (GPS-LEO) occultations, provide an ideal geometry for observing layered structures like E_s with many advantages over GPS-ground links. In order to observe E_s layers, ground-based GPS receivers need to make overhorizon measurements [*Coco et al.*, 1995], which are often contaminated by large multipath errors. The satellite-to-satellite links normally do not have multipath problems with the surrounding environment, provided that the high-rate (50 Hz and 100 Hz) vertical sampling with advanced GPS receivers can adequately resolve thin-layered structures. For satellite-to-satellite links, E_s signals are much stronger than those received during ground-to-satellite links, and contaminations from *F* region fluctuations can be effectively minimized. More importantly, GPS-ground measurements are regional, whereas GPS-LEO occultations are global with ~200–250 daily profiles on a single antenna.

[6] The GPS constellation consists of ~29 satellites (canonically 24 plus a few spares) that are distributed roughly in six circular orbital planes with ~55° inclination at 20,200-km altitude. Each GPS satellite continuously broadcasts at two L-band frequencies: 1.6 (L1) and 1.2 GHz (L2) [*Spilker*, 1980]. Precise measurements of time delay between GPS transmitters and LEO receivers can be used to obtain profiles of atmospheric pressure, temperature, and water vapor [e.g., *Kursinski et al.*, 1997] or electron density [*Hajj and Romans*, 1998]. These profiles generally have good vertical resolution, benefiting from very high sampling rates (e.g., 50 and 100 Hz) in the occultation measurements. Remote sensing of Earth's atmosphere with the GPS occultation technique was first demonstrated in GPS/MET mission during 1995–1997 [*Ware et al.*, 1996]. The recent missions, such as the German Challenging Minisatellite Payload (CHAMP) [*Wickert et al.*, 2001], the Argentinean Satelite de Aplicaciones Cientificas-C (SAC-C) [*Hajj et al.*, 2004], and the Department of Defense Ionospheric Experiment [*Straus et al.*, 2003] are producing a total of ~600 occultations per day. Future GPS occultation missions, such as Constellation Observing System for Meteorology, Ionosphere, and Climate (COSMIC) and Communications/Navigation Outage Forecasting System, will provide over 3000 profiles per day with dense geographical and local time coverage.

[7] This paper describes a novel variance analysis method for extracting E_s information from the signal fluctuations in satellite radio occultations and compiles a climatology of E_s with recent measurements from GPS/CHAMP. The paper is organized as follows: Section 2 describes GPS/CHAMP data collected during 2001–2003 and the analysis method. Section 3 presents the global E_s morphology to show its geographical, vertical, and local time variations. These initial results reveal many interesting features and open the door for further modeling and theoretical investigations. In section 4 we model radio wave propagation through a perturbed ionosphere to characterize the sensitivity of occultation measurements to perturbation vertical and horizontal scales. A conclusion is given in section 5.

2. Data and Analysis

[8] In most applications, high-frequency oscillations in the signal's amplitude (measured by signal-to-noise ratio (SNR)) and phase data are usually treated as measurement noise for its fussy nature and potential degradation to communication quality. This "noise," however, contains valuable information on physical and statistical properties and variabilities about E_s, which can be used to study and understand their occurrences.

[9] The SNR and phase scintillations in satellite-to-satellite links can be directly related to electron density fluctuations associated with E_s. The atmosphere/ionosphere interacts with radio wave propagation through atmospheric refractivity, $N = (n - 1)10^6$, for the index of refraction n. The refractivity depends on atmospheric temperature T, total and water vapor pressure (P and P_w), electron density n_e, and radio frequency f, namely,

$$N = 77.6\frac{P}{T} + 3.73 \times 10^5 \frac{P_w}{T^2} - 4.03 \times 10^7 \frac{n_e}{f^2}, \qquad (1)$$

where P and P_w are in hectopascals, T is in kelvins, n_e is in m^{-3}, and f is in hertz. Important atmospheric/ionospheric effects on the GPS occultation measurements are summarized by *Hajj et al.* [2002] as follows:

2.1. Bending Effect

[10] Atmospheric refraction introduces bending to radio wave propagation from GPS to LEO, causing an excess phase delay. The bending effect increases with air, water vapor, and electron densities. Because of this bending, the signal can be received even when the transmitter is slightly behind the Earth. The bending contributions from air/water are generally small at tangent heights above ~50 km, compared to electron density effects.

2.2. Defocusing/Focusing Effect

[11] Vertical gradients of the bending angle cause the transmitted beam to diverge or converge, which reduces/increases signal power at the area-constant receiver antenna. The defocusing/focusing effect increases with air pressure as the vertical gradient increases, causing the receiver power to decrease gradually with pressure at tangent heights below

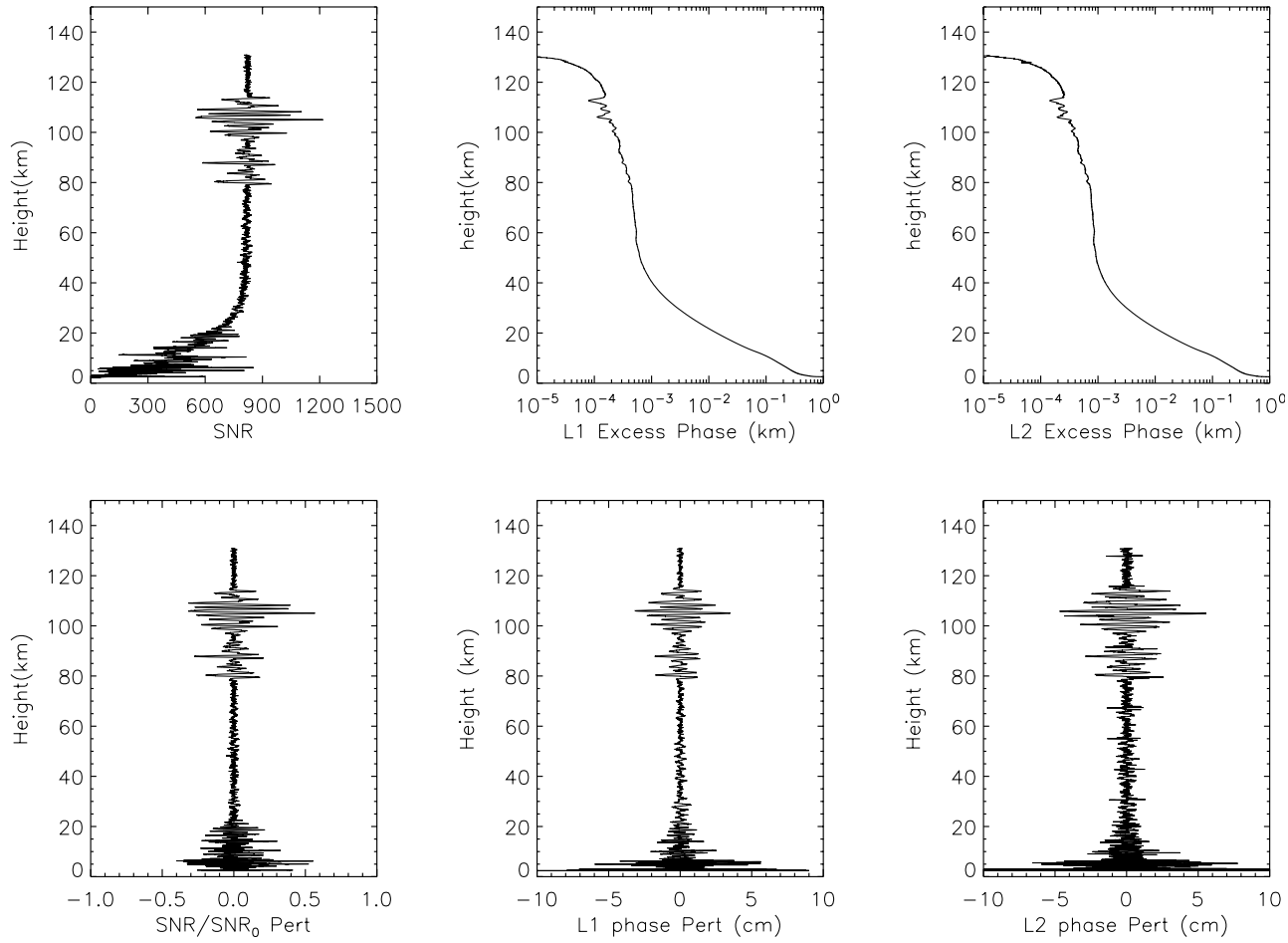

Figure 1. A CHAMP occultation at 50.5°S and 163.9°W on 11 January 2002. (top) The 50-Hz measurements of SNR, L1, and L2 excess phase profiles. (bottom) Perturbation (Pert) of the SNR and phases extracted with a 2-s high-pass filter, where the SNR perturbations are normalized to its free-space average. Filter must be applied twice to the phases to detrend the data.

~30 km. Sharp vertical structures, such as ones near the planetary boundary layer, can even cause a temporary loss of signal.

2.3. Diffraction Effect

[12] Diffraction occurs when the transmitted signal encounters the irregularities of scales near or less than the Fresnel diameter which depends on the transmitted radio wavelength, the transmitter-receiver distance, and the refractivity vertical gradient. For typical GPS-LEO occultation applications (at an 800-km orbit) the Fresnel diameter is ~1.5 km in the *E* region and hundreds of meters in the troposphere.

2.4. Multipath Effect

[13] Very sharp and thin vertical structures in the atmosphere/ionosphere may cause strong differential bending among the transmitted rays. As a result the signals may reach the receiver from different paths. In this case, interference among the rays from different paths must be considered.

[14] E_s-induced scintillations are not new in satellite-satellite communications but are amplified in the high-rate (50 or 100 Hz) GPS occultation observations. Strong E_s features in the high-rate data can be readily extracted after instrument/measurement errors are carefully analyzed. There are many advantages to analyzing the raw SNR and phase measurements instead of retrieved quantities (such as total electron content). First, E_s information can be obtained directly from the high-rate L1 data without smoothing the data, relying on the noisier L2 data, and solving GPS orbits or clocks. Any smoothing on the L1 and L2 data prior to analyses may lose some of the information on small-scale E_s features. Second, traditional retrieval processes (e.g., the Abel inversion) often assume spherical symmetry, which is not valid for E_s structures, and make the retrieved quantities more difficult to interpret [*Hajj and Romans*, 1998]. Third, measurement noise is relatively simple to analyze in the raw data and not subject to various errors introduced during data reduction. This leads to a larger number of useful occultations.

2.5. SNR and Phase Fluctuations

[15] Figure 1 (top) shows the 50-Hz SNR, L1, and L2 phase measurements during a CHAMP occultation in January 2002. Starting from a tangent height of ~140 km, this occultation scans through the *E* region at a descending rate of ~2.2 km/s. In this case the SNR is close to ~800, the free-space value (SNR_0), until the tangent height is below

~40 km. The defocusing effect of the neutral atmosphere begins to play a major role in the lower heights and causes an overall attenuation of the SNR until it vanishes near the Earth's surface. Since the raw data contain phase and SNR as functions of time rather than tangent height, the mapping between time and tangent height was done from knowledge of the satellite ephemeris, assuming the straight line propagation in the ionosphere and upper stratosphere, and using the Abel inversion for bending angle in the lower stratosphere and troposphere.

[16] The SNR fluctuates slightly about SNR_0 above ~50 km for normal quiet ionospheric conditions, but the SNR_0 can vary substantially from occultation to occultation, depending on the viewing angle of the GPS satellite with respect to the LEO antenna. In the normal cases the L1 and L2 excess delays (corrected for satellite motions and clocks) vary gradually at tangent heights above ~40 km due to the weak bending by the ionosphere but increase exponentially below ~40 km due to the strong bending of the neutral atmosphere. In this example (Figure 1), the excess delays and the SNR exhibit abrupt variations at tangent heights between 80 and 120 km, which are indicative of sharp structures in that region.

[17] To extract short-scale SNR and phase perturbations, we first detrend the data with an *N*-point running window. This detrending method outputs the difference between the data sequence and the *N*-point smoothed sequence as a filtered result. It is an equivalent high-passed filtering process where slowly varying or large-scale components are removed. Because the phase measurements vary exponentially with height, this filtering process is applied twice when detrending the phase data.

[18] The detrended data are shown Figure 1 (bottom), where the SNR perturbations are normalized by SNR_0. In this case, large oscillations due to E_s are clearly evident in SNR/SNR_0 and phase perturbations at tangent heights of 80–120 km. The SNR perturbations reach as high as 50%, while L1 and L2 phase perturbations show maxima of 5 and 8 cm, respectively. Both SNR and phase fluctuations reduce substantially at tangent heights between 30 and 70 km, where they are mostly dominated by the measurement noise. In the enhanced E_s region, fluctuations can be much greater than the instrument noise. At tangent heights below ~40 km, fluctuations are dominated by neutral atmospheric variabilities in temperature, pressure, and water vapor, and they are outside the scope of this paper and will be investigated in a separate study.

[19] E_s-induced fluctuations in the SNR, L1, and L2 phase measurements exhibit great coherency in most parts of the E_s event (Figure 2). The correlations between L1 SNR and phase fluctuations are sometimes complicated by the detailed E_s structure, but the L1-L2 phase correlations generally obey the frequency dependence described in equation (1) for electron density perturbations. As shown in Figure 2 (right), the L1 and L2 phase fluctuations are linearly correlated with a slope close to $(f_1/f_2)^2$, where f_1 and f_2 correspond to the L1 and L2 frequencies, respectively. An interesting scenario appears at 103–107 km altitudes where L2 phase oscillations lag L1 by ~150 m. This lag manifests itself as the circular pattern in the L1 and L2 phase correlation (Figure 2 (middle right)), which is likely caused by the frequency-dependent bending associated with sharp vertical structures of these E_s layers. The bending separation between L1 and L2 phase measurements (typically 100–500 m) depends on the vertical gradient of electron density [*Hajj and Romans*, 1998]. Because E_s layers are often thin, large vertical gradients in electron density are readily present over a few kilometers and cause a noticeable separation in the high-rate measurements. By carefully modeling radio waves propagation through highly structured media, it is possible to reconstruct a high-resolution vertical profile of E_s layers from the 50-Hz SNR and phase measurements [*Igarashi et al.*, 2002; *Gorbunov*, 2002; *Ao et al.*, 2003].

2.6. Sampling and Coverage

[20] To cover the typical height range of E_s phenomena (80–120 km), GPS receivers need to start tracking at a tangent height above E_s layers. During the early CHAMP operation in 2001–2002, occultations did not start sufficiently high to sample the entire E_s region. Figure 3 shows that the high-rate occultations were only as high as ~100–110 km before February 2002, which was later raised to 140–150 km specifically for E_s studies.

[21] Normal CHAMP operation produces 200–250 daily occultations, but the number of profiles in the level 2 data is significantly less than that in the level 1 data because of tighter quality controls needed for the level 2 retrievals (i.e., density and temperature profiles in the stratosphere and troposphere). This study uses the SNR and phase data released in the level 2 files, which appear to have a sufficient number of profiles for monthly and seasonal climatologies. In future studies the algorithm will be modified to directly use the level 1 data and hence increase the number of daily occultations.

[22] CHAMP orbit precesses in local time with a rate of ~5.6 min/d at the equator, sampling a complete 24-hour cycle every ~130 days with both ascending and descending nodes. However, this revisit period is not exactly 130 days since occultations are spread by ~2 hours for each node (Figure 4). This spreading is caused by the nature of the GPS-LEO occultation geometry and the broad antenna field of view (~70°) that allows the receiver to view occultations from many directions where GPS satellites may appear. The spreading in local time is more discrete at the equator than at middle and high latitudes. This spread time coverage causes the effective repeat period (for covering 24-hour local time) to be ~108 days and therefore helps slightly to reduce aliasing between diurnal and seasonal variations.

2.7. Variance Analysis and Noise Removal

[23] The SNR and phase fluctuations contain not only E_s perturbations but also instrument/measurement noise and other ionospheric variations at higher altitudes. The instrument/measurement noise sometimes shows up as spikes in SNR and phase perturbations and can vary from occultation to occultation. The deduced variances from SNR and phase measurements, σ^2, can be written as a sum of these sources:

$$\sigma^2 = \sigma^2_{E_s} + \sigma^2_{\varepsilon} + \sigma^2_F, \tag{2}$$

where σ^2_{Es}, σ^2_{ε}, and σ^2_F are respectively E_s, noise, and F region variances. The noise, including instrument radiometric and clock errors, may not completely behave as a

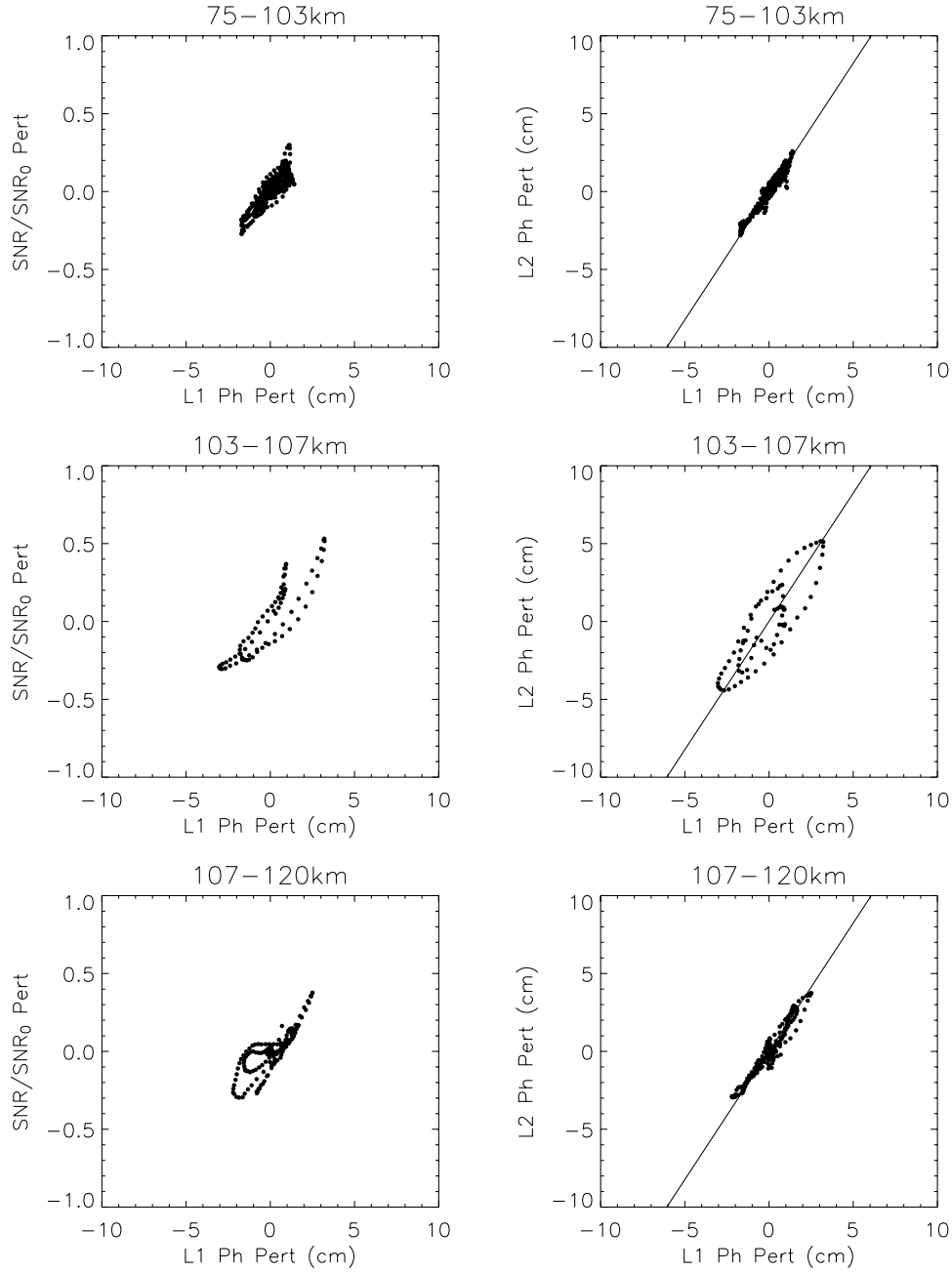

Figure 2. Correlations for (left) SNR phase and (right) L1-L2 phase fluctuations at (top) 75–103, (middle) 103–107, and (bottom) 107–120 km. Dots represents the phase measurements, and the slope is the ratio of L1 and L2 frequencies.

random and stationary sequence. Because these errors vary from occultation to occultation, we must remove them on a profile-by-profile basis. The clock error tends to generate small periodic spikes in the phase data, contributing significant spectral power at high frequencies (>10 Hz). To remove these clock spikes, we apply the three-point high-pass filter to the phase data and subtract the three-point filtered sequence from the *N*-point filtered one. We refer to this process as the (*N*, 3) band-pass filtering. As shown in Figure 5, the (*N*, 3) band filter can significantly reduce the noise power at frequencies >10 Hz, and removing the noise is particularly important for the phase variances where E_s amplitudes are weak.

[24] As the standard variance products, we process the 50-Hz SNR and phase data with several band-pass filters: (401, 3), (201, 3), (101, 3), (51, 3), and (21, 3) to study E_s variabilities at different vertical scales. The noise removal with the three-point filter also helps to eliminate possible *F* region contaminations [*Straus et al.*, 2003]. *F* region fluctuations can generate very noisy measurements over a broad range of tangent heights, extending above and below the E_s region. Profiles are discarded if the averaged three-point variance is 20 times greater than its monthly mean at tangent heights above 120 km or between 40 and 80 km. Furthermore, L1 and L2 phase measurements are analyzed between 40 and 60 km. Because the L2 phase measure-

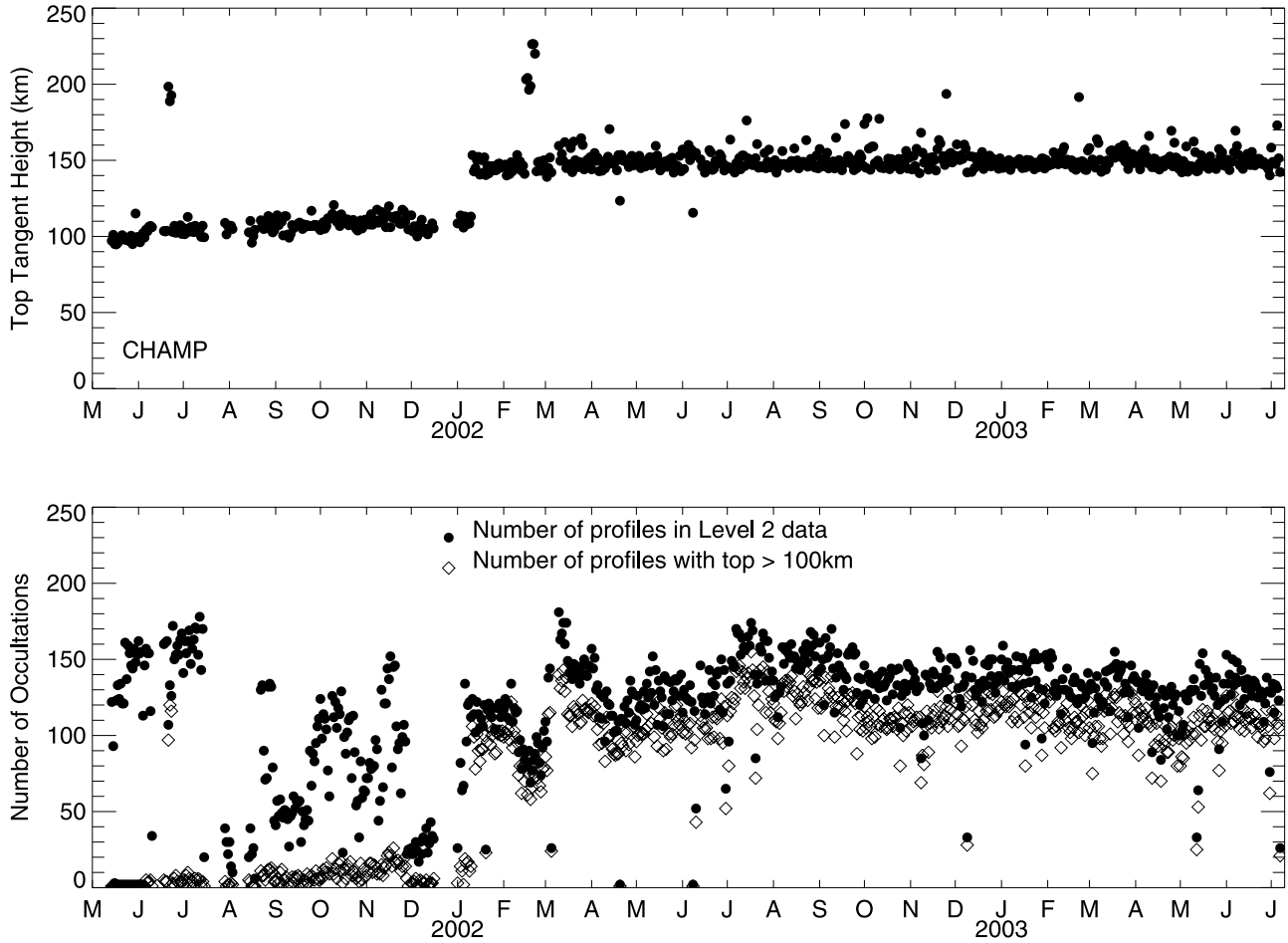

Figure 3. Summary of CHAMP height coverage.

Figure 4. Summary of CHAMP local time coverage at ±45° and at the equator.

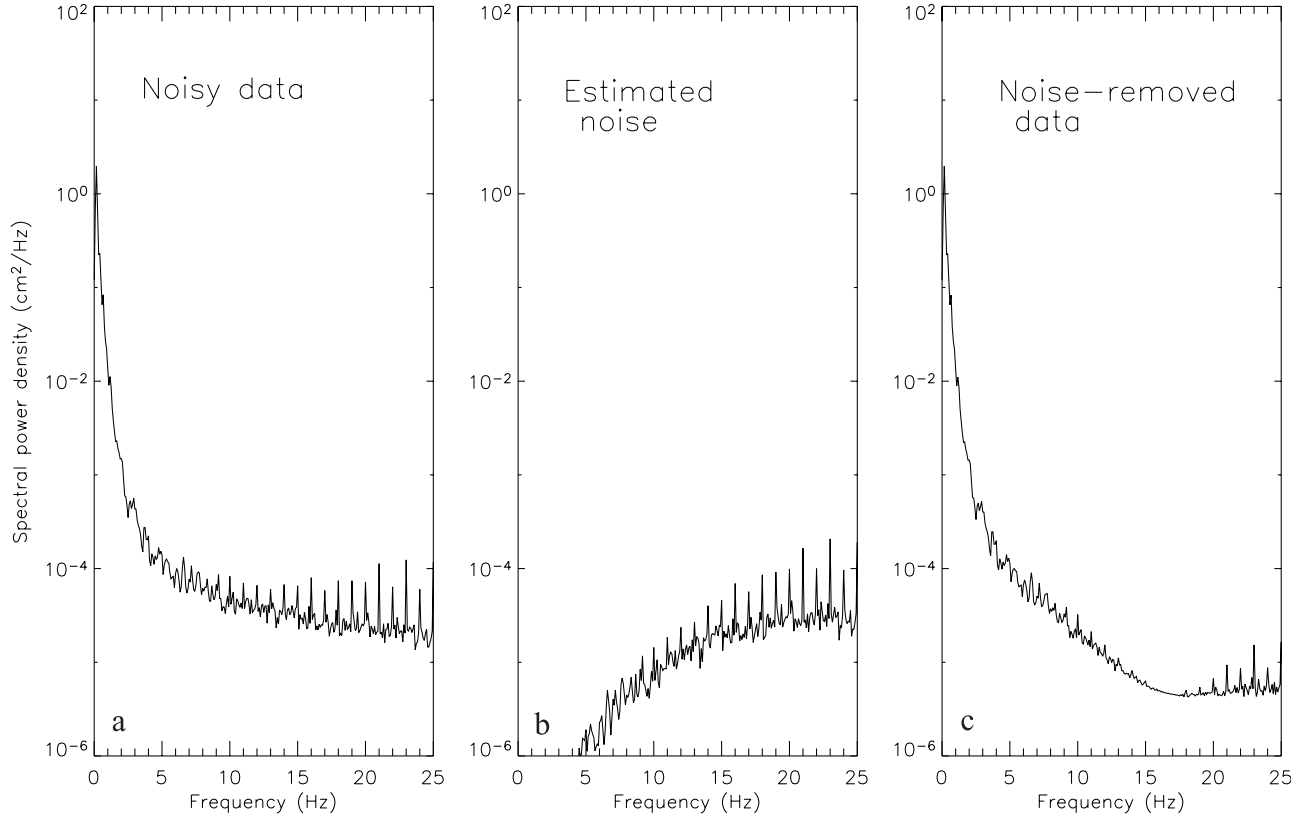

Figure 5. Illustration of noise removed in the variance calculation. This example shows the monthly averaged power spectra for (a) noisy L1 phase perturbations, (b) estimated noise, and (c) noise-filtered phase perturbations using the (401,3) truncation. Instrument/calibration noise exhibits periodic power spikes at frequencies (>10 Hz), which can be estimated and removed to large extent with the three-point high-pass filter as described in the text. In the (401,3) band-pass filtered sequence the noise power at frequencies is substantially suppressed.

ments are noisier than L1, a looser tolerance is applied for L2 quality control.

[25] For CHAMP occultations the 51-point truncation corresponds to a vertical scale of ~2.2 km. The vertical scale used by *Hocke et al.* [2001] is equivalent to the 201-point (or 4 s) truncation. However, there are three key differences between our approach and the one used by *Hocke et al.* [2001]: (1) They did not analyze the SNR data but the horizontal total electron content deduced from L1-L2 phase differences. (2) They chose to measure the average rather than the variance of the fluctuations, which may significantly change the E_s strength and morphology. (3) They did not consider measurement noise or calibration errors in their analysis.

3. Results

3.1. Zonal Means

[26] Monthly mean variances in June 2002 (Figure 6) and January 2003 (Figure 7) show clearly that E_s features dominate the summer hemisphere. The maxima in the SNR and phases fluctuations are aligned with the E_s layers and represent approximately the vertical distribution of E_s variability. The summertime E_s is dominated by activities at altitudes of 80–120 km with the peak at ~105 km near 45°S in January and at ~102 km near 45°N in June. The E_s variances in the summer hemisphere correlate well with the mean zonal wind, which reaches ~40 m/s in the Committee on Space Research (COSPAR) International Reference Atmosphere 1986 climatology. The E_s variances in June appear slightly greater in amplitude than those in January and occur in a broader height range. The E_s variances are much weaker in the winter hemisphere but remain significant in CHAMP phase data. Equatorial E_s variances are generally weak, confined in a narrow altitude region around 100 km, and may be more prominent in June than in January. Besides, large variances at lower altitudes (<20 km) reflect sharp variations of atmospheric refractivity associated with temperature and water vapor changes in the troposphere.

3.2. Seasonal Variations

[27] Figure 8 shows the daily averages of CHAMP SNR and phase variances for an annual cycle using data collected between May 2001 and July 2003. Both ascending and descending samples are used for averaging so as to reduce the aliasing effects from diurnal variations. However, semidiurnal and seasonal variations can still alias to each other, which could explain the periodical (~65 days) modulations seen in the seasonal variations.

[28] As shown in Figure 8, the E_s variances exhibit strong seasonal variations at all latitudes and have slightly different morphologies at 95, 105, and 112 km. Near 95 km, midlatitude E_s activities in the Northern Hemisphere (NH) last 6 months from April to October, and the largest

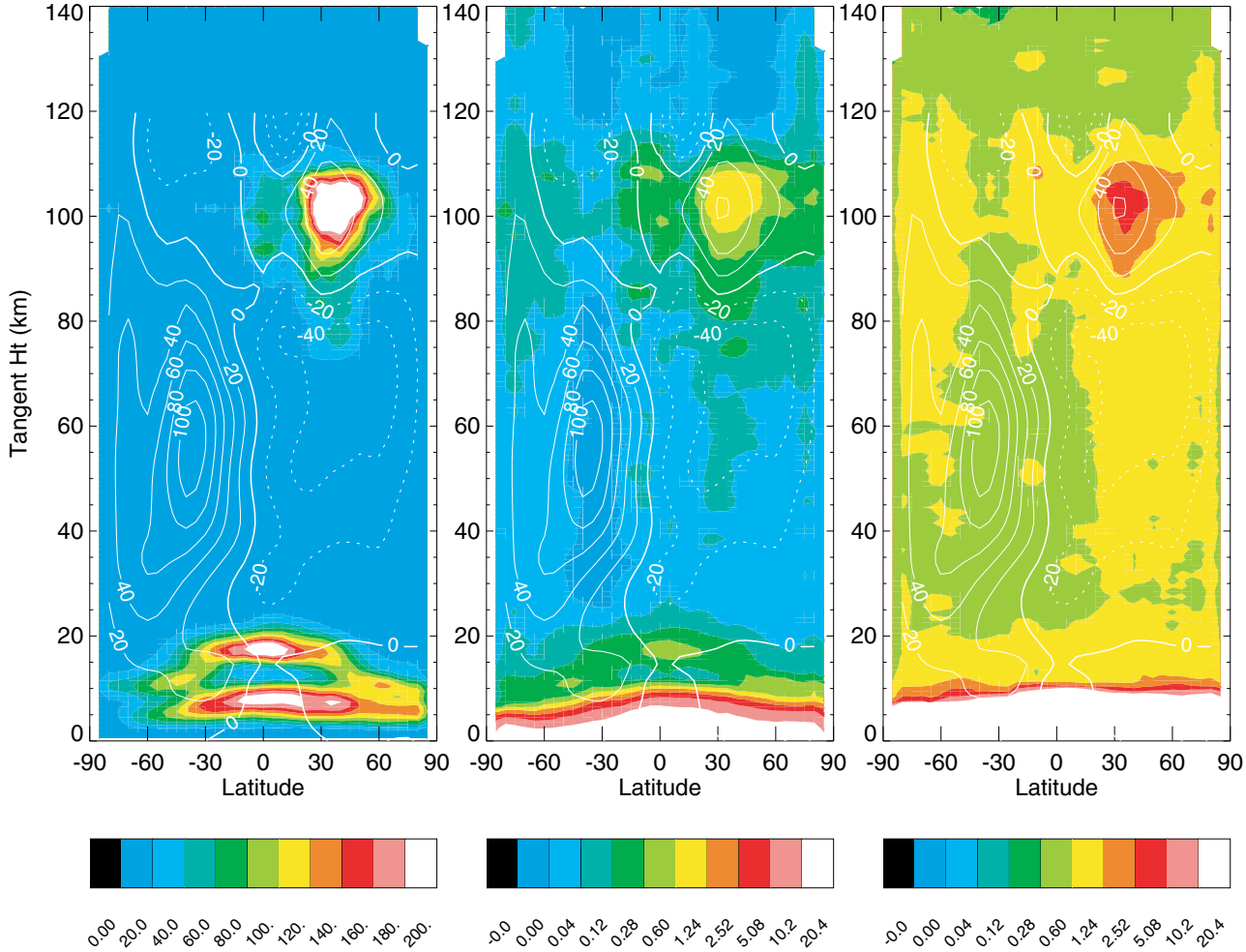

Figure 6. Zonal mean variances in CHAMP SNR, L1, and L2 phases for fluctuations <1 s (or vertical wavelength less than ~2 km) during June 2002. Latitude and height (Ht) bins are 5° and 1 km, respectively. Color scales are $(\%)^2$ for the SNR/SNR_0 variance and cm^2 for the L1 and L2 phase variances. Contours are the Committee on Space Research (COSPAR) International Reference Atmosphere 1986 climatology for zonal mean wind.

variance appears in late May and early June. The peak variance moves in latitude from ~20°N in April to ~40°N in June and back to ~20°N in August before shifting to ~40°N again in September. The NH high-latitude (around 75°N) activity prevails in almost all seasons except for the short break in March. The midlatitude E_s activities in the Southern Hemisphere (SH) occur mostly in October and November with many weaker enhancements spread over other periods (January–February, April, and September). The SH high-latitude (around 60°S) variances are spread between October and February with the most active ones in December and January.

[29] At 105 km, where the E_s variances are strongest, the NH midlatitude E_s shows greater enhancements during May–August and peaks in mid-June. At the NH high latitudes, E_s activity appears mainly in the off-summer months (October–March), and the summertime activity is diminished compared to the one at 95 km. In the SH the middle and high-latitude activities are blurred together during the October–March period, and weak variances are present near ~60°S for the rest of the period. Equatorial E_s activities are significant for the January–February, May–June, and August–October periods.

[30] At 112 km the seasonal variation of the NH midlatitude E_s varies not only with time but also with latitude as the maximum shifts from 30°N in May to ~50°N in late July. The strongest variance here occurs in late July and early August, further delayed from the peak times at the lower heights. The NH high-latitude activity becomes weaker but remains significant over the period from October to March. The SH E_s activities are split into two periods (November–December and January–February) with the stronger one in the first period. The equatorial E_s in late January and early February remain more prominent than those during the transition (equinoctial) periods.

3.3. E_s Variance Maps

[31] The GPS-LEO occultation technique can provide global maps of E_s variances, which are important for studying the dependence of E_s on the horizontal winds

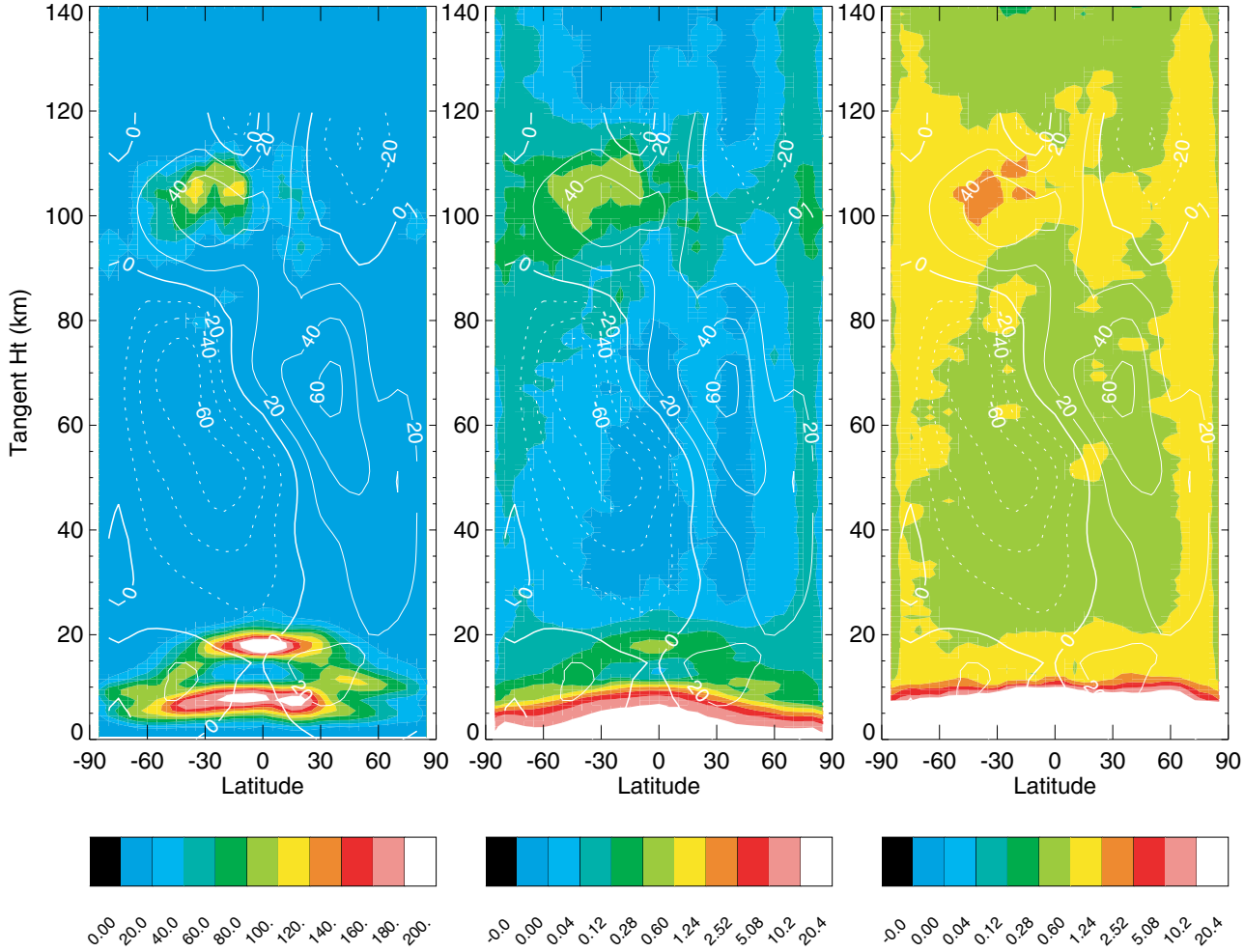

Figure 7. Same as Figure 6 except for January 2003.

and the geomagnetic field. Figure 9 shows the 105-km maps of L1 SNR/SNR$_0$ and phase variances during (a) June–August 2002 (JJA) and (b) December 2002 to February 2003 (DJF) when the summertime E_s are maximized. These maps reflect the stationary component of E_s at planetary scales that may be related to the geomagnetic field. Because CHAMP satellite drifts slowly in local time as shown in Figure 4, the 3-month averages can be contaminated somewhat by fast-traveling planetary waves.

[32] In JJA (Figure 9a), E_s irregularities appear strongly in the summer hemisphere, mostly over China, northwestern Pacific, western United States, northern Atlantic, and southern Europe. However, they mostly fall into the latitude band where the geomagnetic field dip angles are between 30° and 70°. This dip angle dependence is quite striking for the summertime activities as they move north and south in latitude following the dip angle changes. The strong longitudinal variations in the 30°–70° dip angle band can not be simply related to the geomagnetic field. Other variabilities, such the horizontal winds and ion sources, must be taken into account. The wintertime E_s activities in JJA are weak and coincide mostly with the dip angles >80°, the southern polar cap with open geomagnetic field lines. Patchy E_s activities are evident in the phase variance at dip angles >80° in the summer pole. Equatorial E_s activities are generally weak and patchy, not showing any dependence on the geomagnetic equator.

[33] In DJF (Figure 9b) the strongest summertime E_s activity is over southern Pacific with variances as high as $\sim(150\%)^2$ in SNR/SNR$_0$ and $\sim$1.6 cm^2 in L1 phase. Other active regions are over the southern Andes and the east and west Australian coasts. In the region south to Indian Ocean and South Africa (between 30° and 60°S), there is a weak but significant E_s appearance. Also showing the strong dip angle dependence, the enhanced variances are basically confined to the 20°–60° latitude band, whereas the weak variances occur almost everywhere in the summer hemisphere. In the winter hemisphere, again, E_s activities become weak and mostly restricted to the region of dip angles >80°.

3.4. Diurnal Cycle

[34] To study the local time variation of E_s activity, we use 3 months of CHAMP data and average them into each hourly bin. Latitudinal and height dependence of E_s diurnal cycle is of particular interest for studying potential tidal influences because of unique neutral wind shears associated with the tides. During the JJA season the summer midlatitude E_s exhibits a strong semidiurnal variation at 105 km with peaks around 1000 and 2000 local solar time (LST)

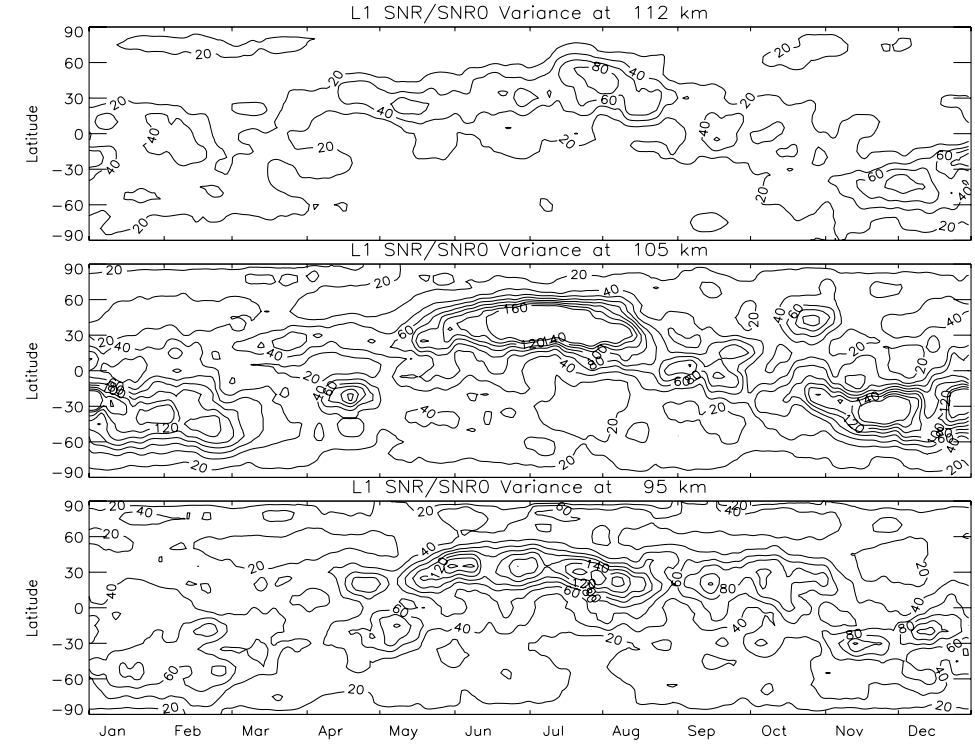

(a)

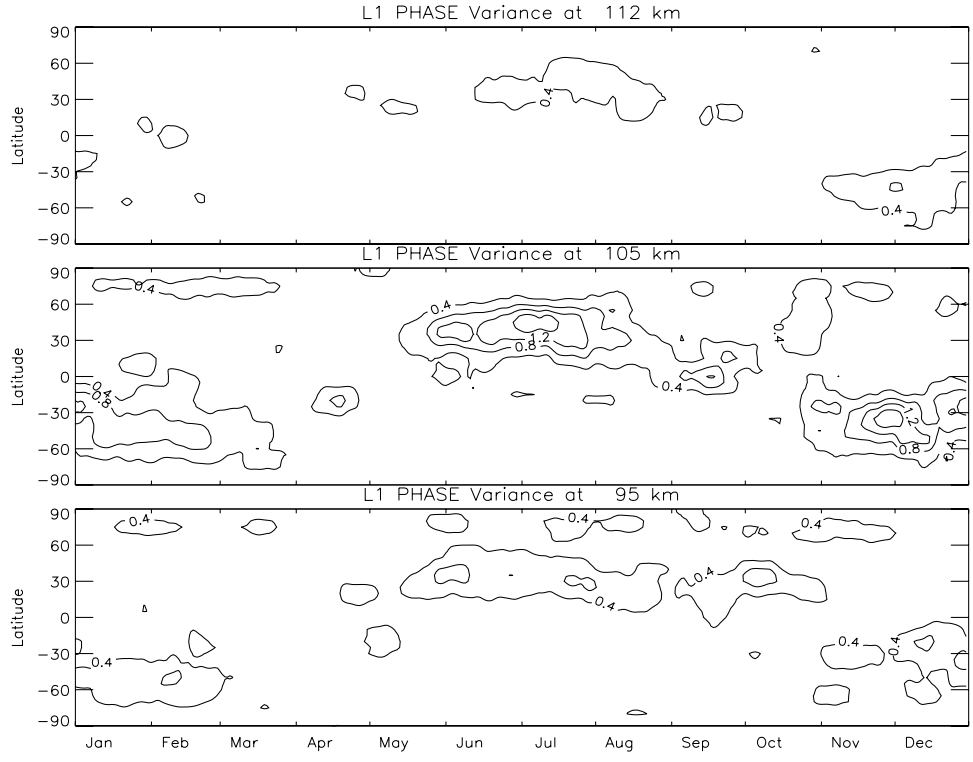

(b)

Figure 8. Latitude-dependent seasonal variations of (a) CHAMP SNR/SNR_0 and (b) phase variances at 95, 105, and 112 km with a 2-km bin. The 51-point variances from the period of May 2001 to July 2003 are used to average out sampling gaps and short-term variability. A 15-day smoothing is applied to the daily averages. Contour scales are $(\%)^2$ for the SNR/SNR_0 variance and cm^2 for the L1 and L2 phase variances.

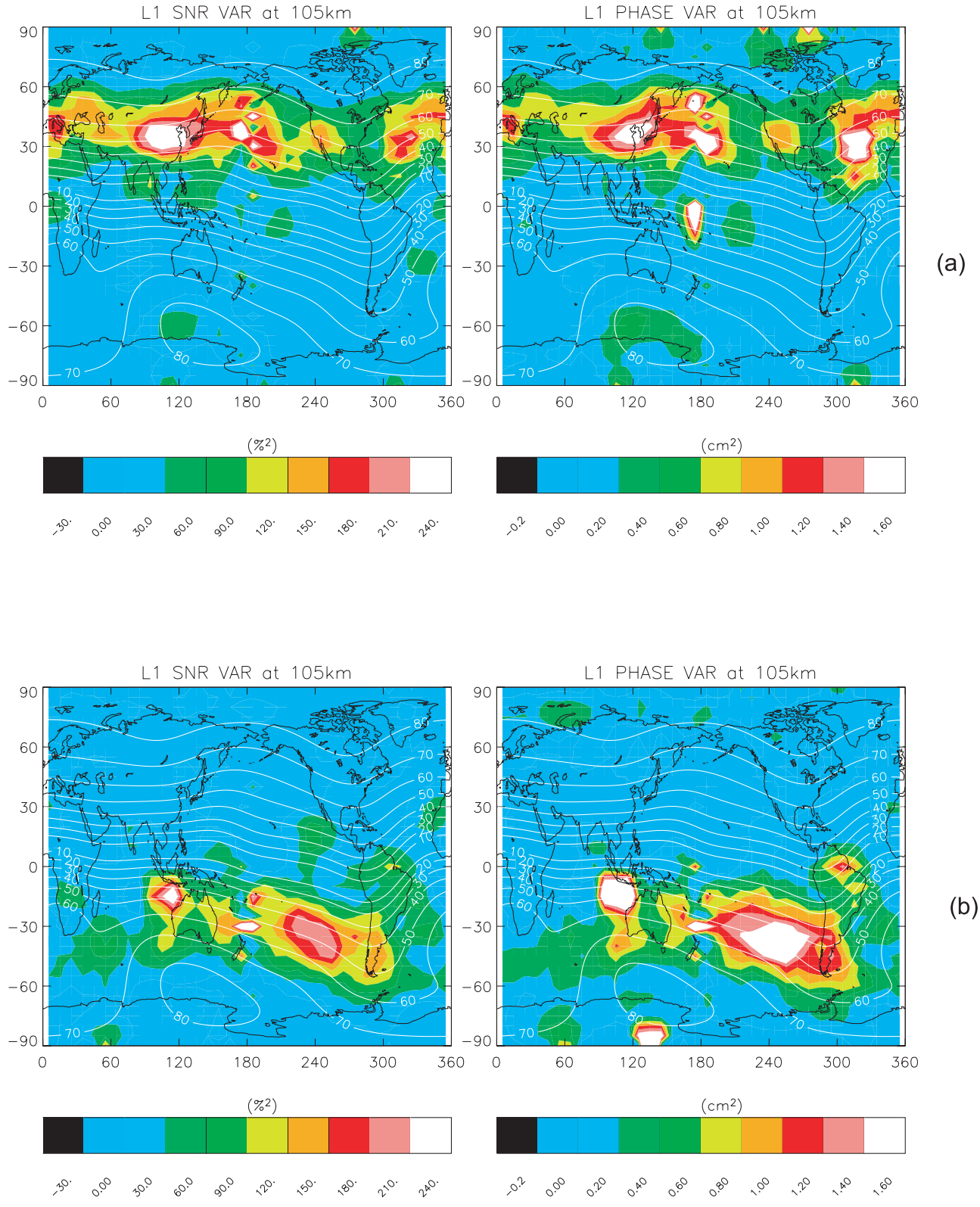

Figure 9. L1 Maps of SNR/SNR$_0$ and phase variances at 100–110 km for (a) June–August 2002 and (b) December 2002 to February 2003. Map has a grid box size of 5° × 10° in latitude by longitude and is smoothed with a three-point averaging. White contours, in degrees, are plotted to show the variations of geomagnetic field dip angle at 105 km.

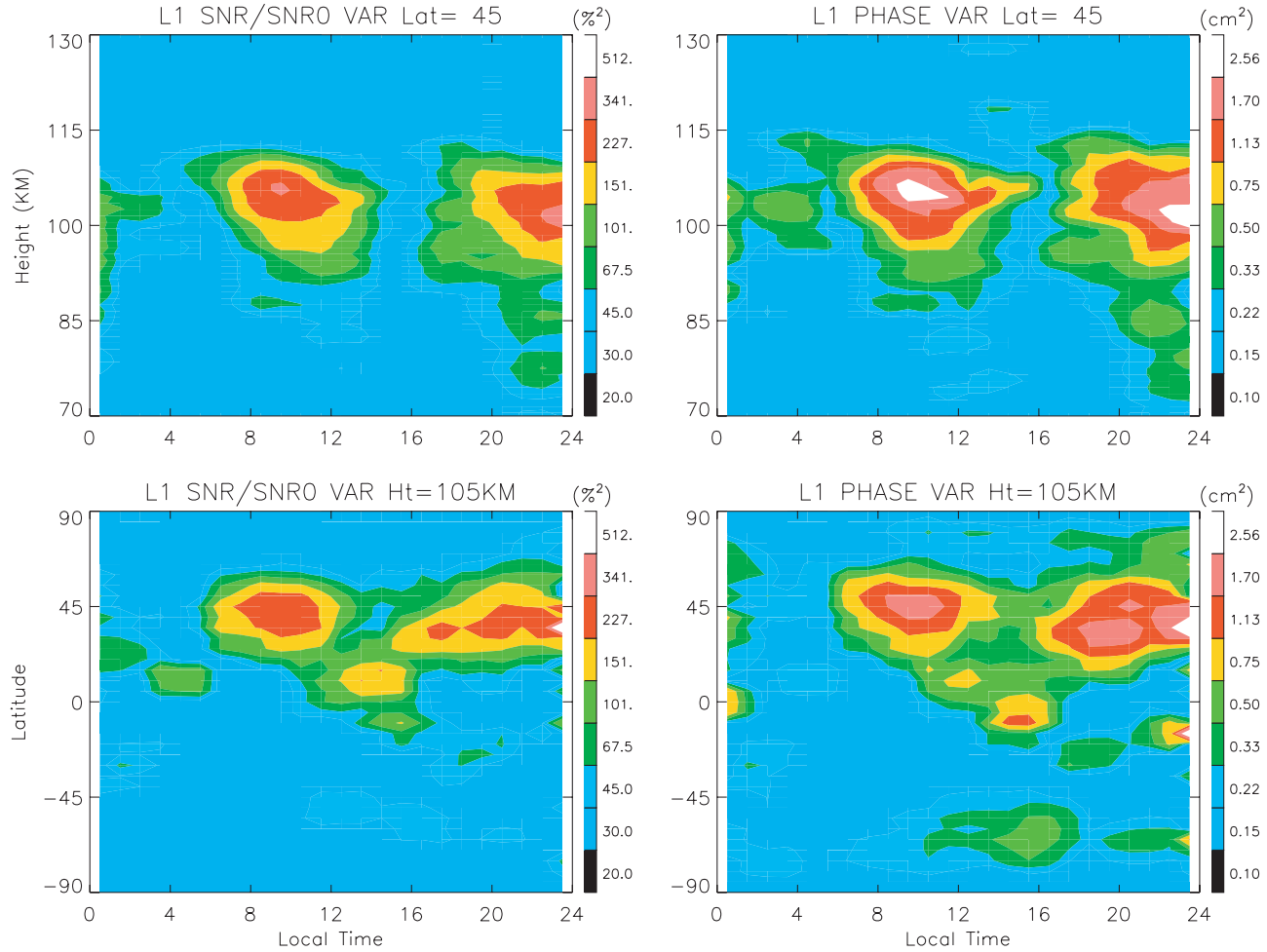

Figure 10. Local time variations of the CHAMP E_s variances in JJA 2002. (top) Time-height view at 45°N; (bottom) time-latitude view at 105 km.

(Figure 10). The semidiurnal variation in the CHAMP variances is generally consistent with ground-based observations from a number of sites in the NH [*Whitehead*, 1989]. Figure 10 also shows a downward progression with height at 45°N in both SNR and phase variances at 70–115 km. Equatorial E_s and the wintertime activities, on the other hand, are dominated by a diurnal variation, showing the peak time between 1400 and 1800 LST.

[35] In DJF (Figure 11) the diurnal variation dominates summertime E_s activities with the maximum enhancement around 2000 LST. In the winter hemisphere, E_s activity is still dominated by a semidiurnal variation with maximums around 0800 and 2000 LST. Equatorial E_s is weak with a diurnal variation and peaks around 1800 LST. The time-height relation at 45°S reveals only slight downward progression for the enhancement near 2000 LST.

4. Simulation of *E* Region Radio Occultation Scintillations

[36] To better understand the SNR and phase variances, we carry out a series of radio wave propagation calculations using a multiple phase screen model to simulate the SNR and phase fluctuations under observing conditions similar to those in GPS-CHAMP occultations. The simulated SNR and phase fluctuations are analyzed with the same variance method to study the sensitivity of GPS occultation to layered ionospheric structures.

4.1. Multiple Phase Screen (MPS) Model

[37] The MPS model in this study uses an effective approach for solving the propagation properties of radio waves through the atmosphere [*Levy*, 2000]. It divides the atmosphere into a series of "phase screens" where the propagating signal is delayed subsequently by an amount determined from the index of refraction at those locations. From one phase screen to the next, the wave propagates as if in vacuum. Computational parameters, including the distance between phase screens as well as the spacing between discretization points in each phase screen, are adjustable according to the needs for model resolution.

[38] The MPS model can compute diffraction effects from sub-Fresnel-scale structures and produce accurate amplitude and phase in the presence of atmospheric multipath structures. It has been widely used for wave scintillation calculations through atmospheric turbulence [*Martin and Flatté*, 1988] and is the de facto standard for simulating GPS occultations. The model and geometric parameters are cho-

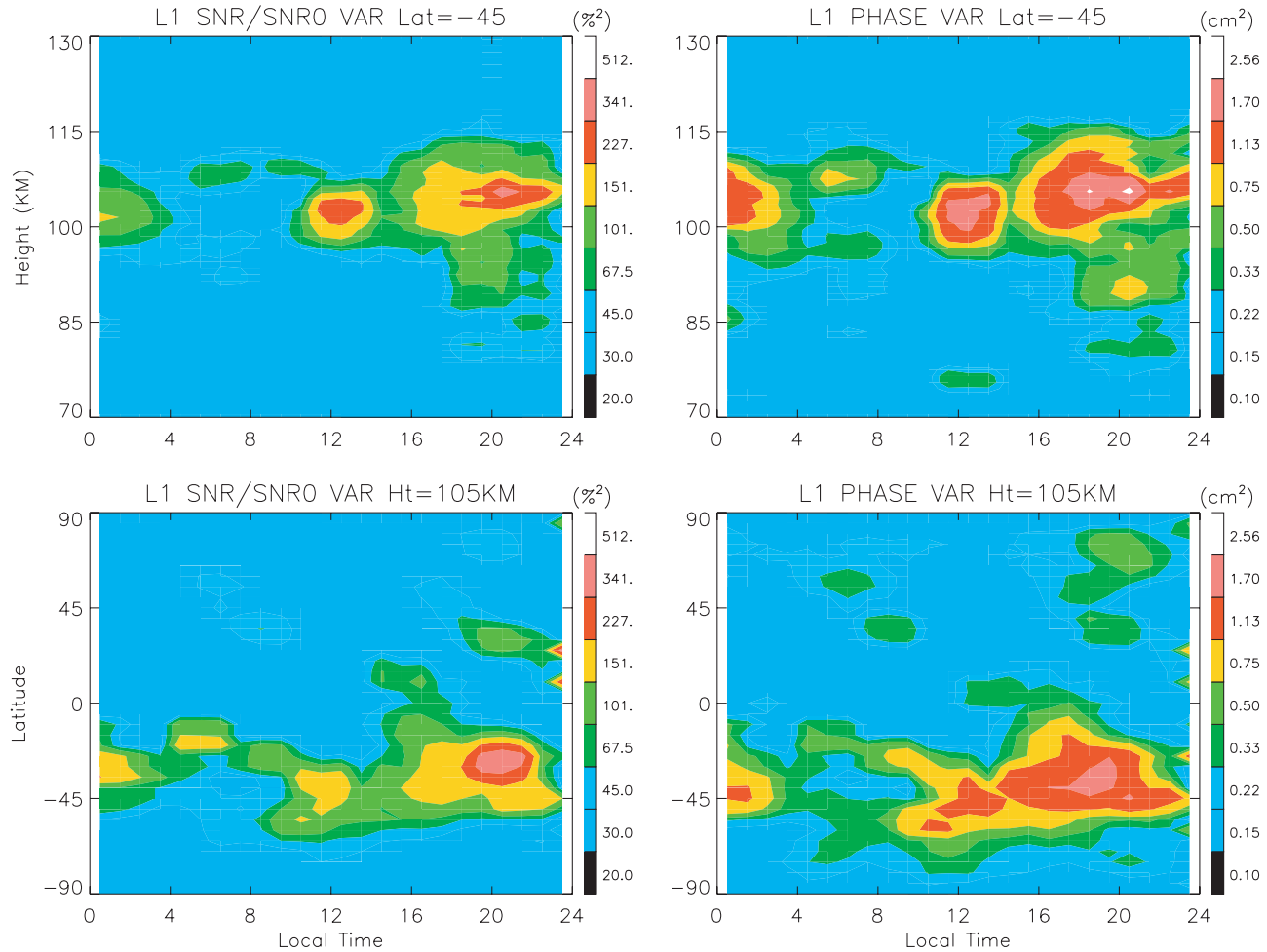

Figure 11. Similar to Figure 10 except for December 2002 to February 2003.

sen as by *Sokolovskiy* [2001] to ensure that the refractivity structures considered here are adequately resolved.

4.2. Simulations of SNR and Phase Fluctuations

[39] In simulating E_s-induced scintillations, we insert wave-like refractivity perturbations near the 100-km altitude and compute signal SNR and phase sequences along the sampling path similar to the CHAMP instrument. We then calculate the SNR and phase variances using the same method as described in section 2 for the real data. The SNR and phase variances are studied against various input perturbation parameters. Most important is the variance dependence on the vertical and horizontal perturbation scales. This property is critical for interpreting the E_s variances observed by CHAMP. In the presence of both horizontally and vertically varying structures, the long line of sight (LOS) path associated with GPS occultation may impose strong smoothing on the E_s layers, making small-scale and localized layers undistinguishable. Similarly, altitude and orientation of thin E_s layers with respect to the LOS direction can change the variance substantially, all of which can be investigated in detail with the MPS model.

[40] In the first set of simulations (Figure 12a) a packet of perturbing layers (with a Gaussian envelop) in terms of refractivity are inserted near the ~100-km altitude. All the perturbing layers are parallel spherical shells with the same horizontal lengths centered at the tangent point. Three horizontal lengths (200, 400, and 1000 km) and seven vertical wavelengths (0.1, 0.2, 0.5, 1, 2, 4, and 8 km) are used for the sensitivity study, and as an example, the results for 200 km are shown in Figure 13. For short vertical wavelengths (0.1 and 0.2 km) the MPS model produces some fuzzy SNR and phase fluctuations at subkilometer scales. Note that these fluctuations are confined mostly in the height region where the perturbation is inserted with a broader spread in the cases of shorter vertical wavelengths (0.1 and 0.2 km). In fact, the SNR and phase responses to the E_s-like perturbations depend largely on the vertical wavelength of the layers inserted. Such scale dependence in SNR and phase variances, which we call the "observational filter," is an important property to characterize the sensitivity of occultation techniques to layered perturbations. For the cases of horizontal scales of 400 and 1000 km (not shown) the SNR and phase fluctuations are evident at lower tangent heights due to the extension of thin layers, which reside quite far away from the tangent point. When E_s layers extend uniformly over several hundred kilometers, spherical symmetry can be applied to retrieve sub-Fresnel structures of the refractivity perturbations using methods

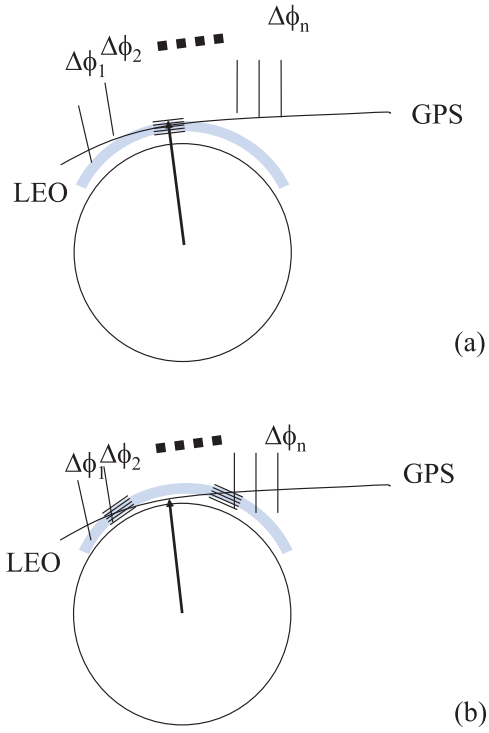

Figure 12. Illustration of the multiple phase screen (MPS) model simulations with artificial wavy perturbation placed (a) near the tangent point and (b) symmetric but far away from the tangent point. Multiple phase screens, spaced between the transmitter and the receiver, are used in the radiative transfer calculation.

like the canonical transform [*Gorbunov*, 2002] or radio holography [*Igarashi et al.*, 2002]. However, the reality is associated with nonuniform layers with patchy distribution in between. The next set of simulations illustrates the effects of horizontally inhomogeneous layers.

[41] In the second group of simulations (Figure 12b) we split the perturbing layers into two parts and place them symmetrically about the tangent point with a gap (~1000 km) in between. Like the first set of simulations the packet of perturbations is placed near 100-km altitude. Now the simulated E_s fluctuations appear at the tangent heights below 100 km as the LOS still intersects with these layers when tangent heights are below 100 km. However, influence of the far-side E_s layers on SNR and phase decreases rapidly as the tangent height descends because the LOS is intersecting these layers at increasing angles (in other words, causing less diffraction). These simulation results imply that the SNR and phase variances must be treated with caution as the ambiguity arises from small-scale inhomogeneous horizontal and vertical structures.

4.3. Observational Filters

[42] Observational filters also point out limitations associated with the radio occultation technique in terms of resolving vertical and horizontal scales of E_s layers. Compared to ground-based techniques, which offer good vertical resolution and time coverage, GPS occultation technique can provide a comparable vertical resolution but coarse horizontal resolution. To quantify the sensitivity of the SNR and phase measurements to ionospheric fluctuations, we define the "observational filter" as the variance response to perturbations of different vertical or horizontal scales and compute these filter functions from the simulations with the MPS model.

[43] Figure 14 shows the "1-s observational filters" of CHAMP SNR and phase variances as a function of perturbation vertical wavelength. Because the other input perturbations are held constant, the variance responses in Figure 14 depict mainly effects of the perturbation vertical wavelength on the SNR and phase variances. Each of these filter functions has a characteristic vertical scale where the variance maximizes. In the SNR case the variance response maximizes for perturbations at a vertical wavelength of ~1.2 km, whereas in the phase case it is ~2 km. It is interesting to note that the characteristic scale of 1.2 km in the SNR response is insensitive to the truncation length used (i.e., 51 points), which is very different from the phase variance response. The characteristic scale of the phase response shifts to a greater vertical wavelength for larger truncation lengths. Hence the phase variances can be used to infer the vertical wavelength spectrum of E_s power, which would be an interesting study in the future.

[44] The characteristic scale of observational filter is determined by the method used to compute the variance and by the physical processes (such as focusing/defocusing, refraction, and diffraction effects) affecting radio wave propagation. At small scales the SNR and phase variances are controlled by the diffraction effect of the perturbing layers, which tend to spread the perturbation power to a broader height (or angular) range in the observing plane, causing both reduced SNR and phase variances. Such spreading effect can be seen in the 0.2-km case of Figure 13. At large scales the phase variance is tapered by the truncation length used in the variance analysis. The characteristic scale of the phase variance is a result of the filtering at both large and small scales, but it increases with the truncation length as more power is allowed from long wavelengths. On the other hand, the SNR variances at large scales are determined primarily by the vertical gradient of refractivity perturbations [*Karayel and Hinson*, 1997] and depend weakly on the truncation length used. As a result the SNR variance decreases with vertical wavelength ($\sim\lambda_z^{-2}$ if horizontal E_s scales are held constant) to yield the unique characteristic scale of ~1.2 km.

5. Discussions

[45] The preliminary E_s climatology from CHAMP ratio occultation is generally consistent with reports from ground-based observations. Global E_s variance maps from CHAMP exhibit clear dependence on the geomagnetic dip angle and the horizontal winds. Most of the midlatitude E_s variances can be qualitatively explained within the framework of the classical wind shear theory [*Whitehead*, 1961], whereas the high-latitude variances remain to be investigated thoroughly. More physical modeling work is needed to make realistic comparisons between the observed and modeled E_s morphologies in the midlatitudes. In addition to the horizontal winds, impacts from other ionospheric and atmospheric variables must be considered, including magnetic field orientations, ion-neutral collision, electric field,

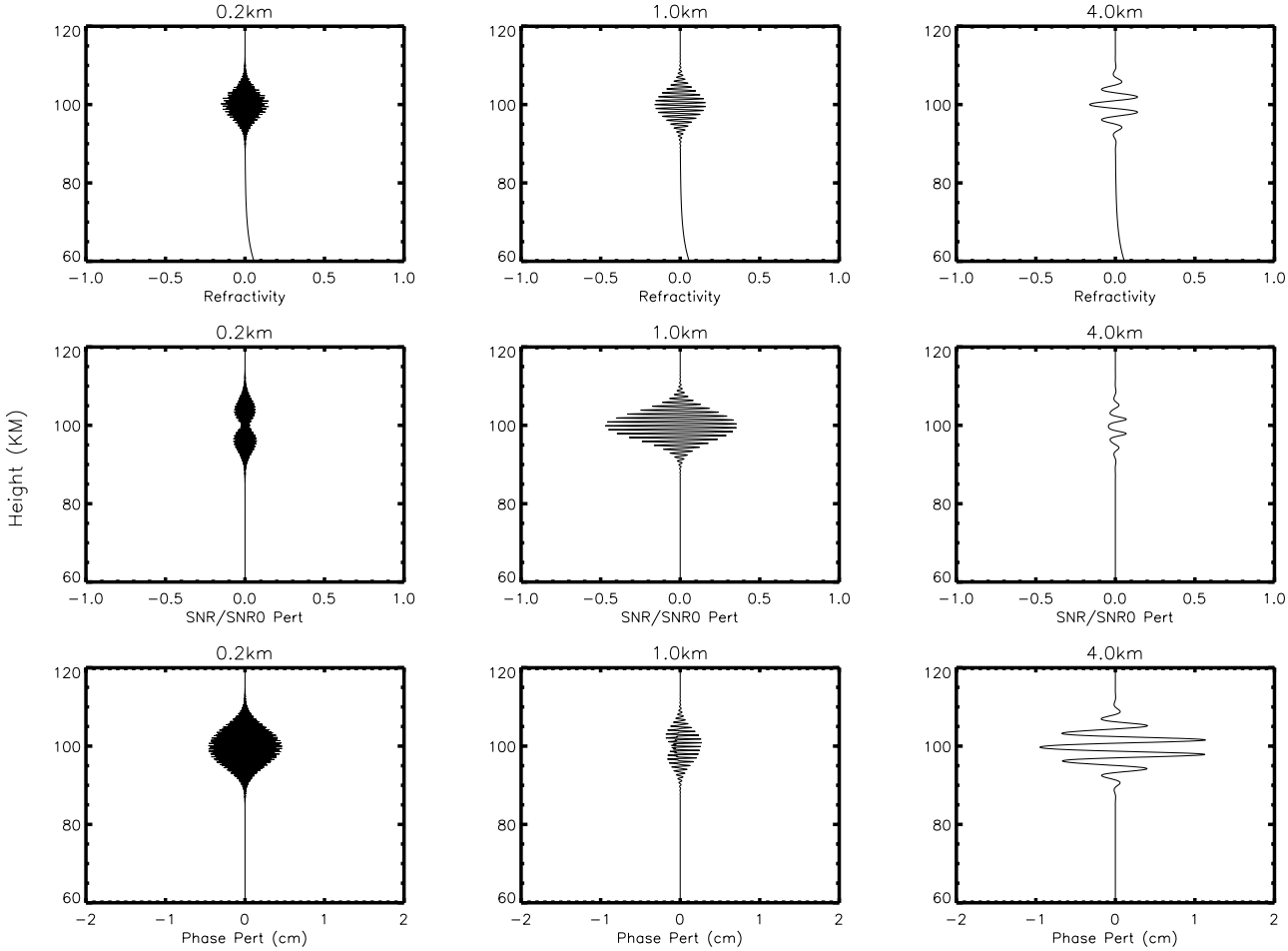

Figure 13. MPS model simulations for the perturbation setting described in Figure 12, where (top) refractive index profiles are shown. L1 (middle) SNR perturbations and (bottom) phase perturbations were detrended in the same way with the 1-s filter as aforementioned for CHAMP data. Three perturbation cases with vertical wavelength (left) 0.2, (middle) 1, and (right) 4 km, are shown. Instrument/calibration noise is not considered in these simulations.

and ion sources. A simple model for E_s layer generation [*Mathews*, 1998], which is based on the wind shear theory but neglecting electric and eastward magnetic fields, expresses the ion vertical velocity in the form as follows:

$$w_z = \frac{1}{1+\gamma^2}(V\cos I\sin I + \gamma U\cos I), \tag{3}$$

where γ is the ratio of ion-neutral collision frequency to ion gyrofrequency, I is the geomagnetic dip angle, U and V are the zonal and meridional winds. It is generally believed that the zonal (meridional) wind is more efficient to affect ion motions at altitudes below (above) ~130 km as the ratio γ becomes greater (smaller) than unity. Nevertheless, γ can vary largely with height at 100–150 km altitudes as well as with latitude. Such transition is evident in global model simulations with realistic horizontal winds [*Carter and Forbes*, 1999].

[46] The dip angle-dependent E_s variances from CHAMP suggest that the influence of the meridional wind might extend far below 130 km. As seen in both DJF and JJA seasons, the E_s variances appear to maximize near $|I| = 45°$, which agrees with the maximum produced from the first term in (3). In other words, the geomagnetic field-controlled conductivity may play a dominant role in the formation of E_s layers. In addition, the local time variation of these variances seems also consistent with the strong influence of the meridional wind. The 1000 and 2000 LST peaks are in phase with the semidiurnal nodes of the meridional wind at 105 km [*Zhang et al.*, 2003], suggesting that the semidiurnal tide might play a direct role in modulating the E_s layers at 100 km. However, the global model simulations [*Carter and Forbes*, 1999] did not show the extended influence of the semidiurnal tide at 100 km where only a diurnal variation is present. Clearly, the CHAMP observations can be used as strong constraints on these physical models to refine the mechanisms that control E_s. Our speculation about the semidiurnal tidal modulation in the E_s variances is a simplistic explanation and does not consider potential influences from other variables, such as electric field and eastward component of the geomagnetic field.

[47] Above ~110 km the E_s variances from CHAMP reduce sharply at summertime midlatitudes, implying a lack of layered electron density structures at 110–140 km (the nominal top of occultation profiles). A question imme-

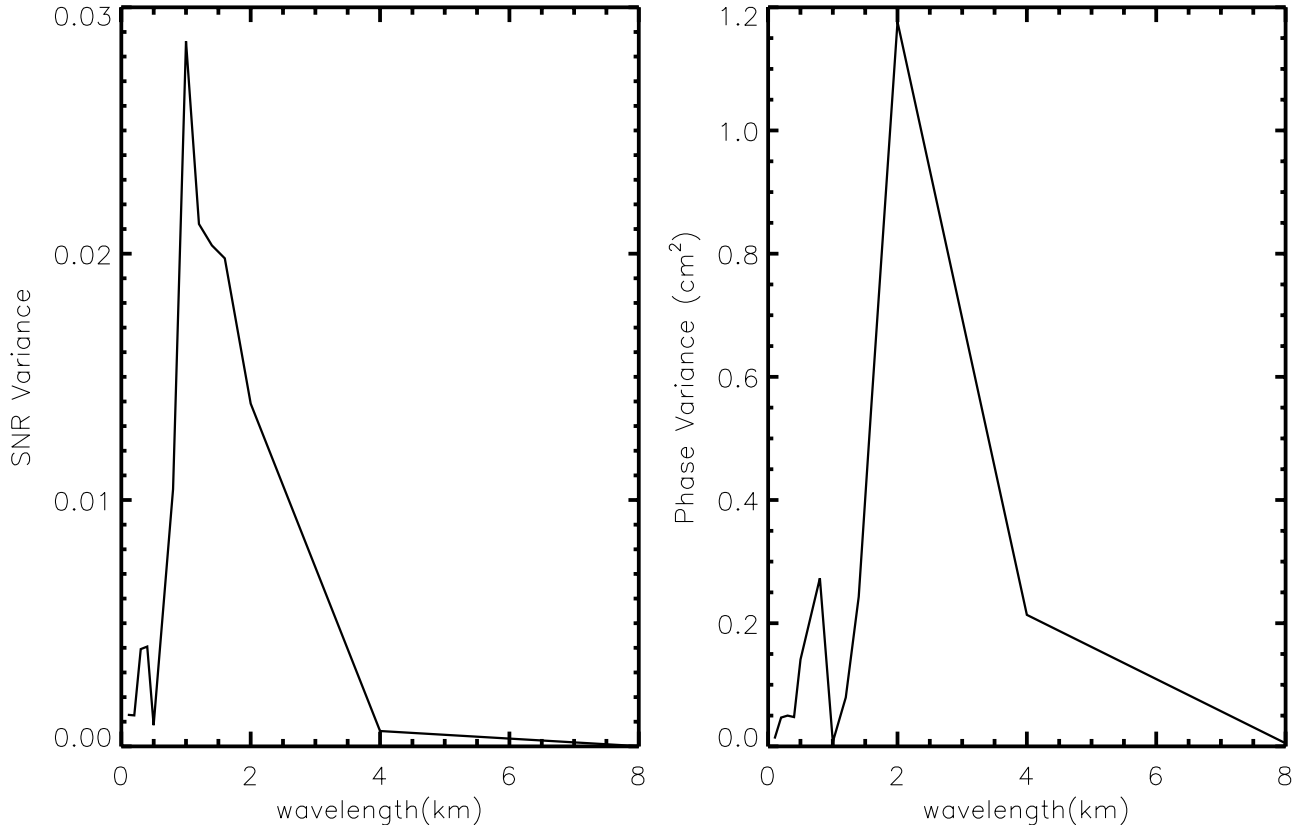

Figure 14. Simulated SNR and phase variances at 90–110 km as a function of vertical wavelength of perturbations put in. The 1-s high-pass filter was used to derive the variances, and the SNR variance is normalized by free-space SNR_0. SNR maximizes its variance response at a vertical wavelength of ~1.2 km, which is independent of the high-pass filter used. On the other hand, the phase maximizes at ~2 km, which would double if the 2-s filter were used.

diately arises regarding the so-called intermediate layer, a descending ion layer from the bottom *F* region and often observed in Arecibo and other radar data [e.g., *Mathews et al.*, 1993]. Some numerical models have reproduced these descending layers by imposing tidal-like modulations in the horizontal winds [*Earle et al.*, 1998; *Carter and Forbes*, 1999]. However, the signatures of these descending ion layers are absent in CHAMP E_s variances. One explanation is that these intermediate layers might be transient, lacking stability and coherency (over tens to hundreds of kilometers) to produce scintillations in the CHAMP data. As indicated in radar observations, these intermediate layers exhibit various stabilities and tend to fluctuate frequently over a much shorter timescale while descending. Thus the occultation technique may not be suitable for observing electron density fluctuations associated with these intermediate layers.

[48] For the similar reason, small-scale field-aligned perturbations, like those due to gravity wave perturbations, are difficult for the GPS occultation technique to detect. As observed in ground-based radar echoes, these field-aligned oscillations are often embedded in E_s layers and have horizontal scales of tens of kilometers and temporal scales of minutes. The long LOS path of GPS occultation will likely smear out most fluctuations of these kinds.

[49] The CHAMP orbit is not ideal for sampling diurnal variations because of the long revisiting period (108 days). The CHAMP sampling can hardly resolve the aliasing between seasonal and diurnal/semidiurnal variations. In studying the diurnal variation, we carefully chose a period when the E_s variances are large and relatively stable over a 3-month period. This allowed us to deduce the semidiurnal variation without being significantly influenced by the seasonal variation. However, the strong diurnal/semidiurnal variations become a problem when studying the seasonal variations, causing an artificial modulation in the latter due to the CHAMP sampling cycle (Figure 8). Combining the measurements from ascending and descending orbits helps reduce impacts of the diurnal variation, but the seasonal variation remains aliased to the semidiurnal variation (the dominant component of E_s). Multiyear averaging may remove some of the semidiurnal influence on the seasonal variation by taking advantages of uncorrelated semidiurnal phases from year to year. An effective way to improve local time sampling is to combine existing SAC/C (Sun-synchronous) and CHAMP measurements. Complete removal of the aliasing between the seasonal and semidiurnal variations requires a better sampling which will become available with future missions such as COSMIC (six receiver satellites) or Equator Atmosphere Research Satellite in a low-inclination rapid precession orbit.

[50] Finally, CHAMP E_s variances in the enhanced regions are often significantly greater than the instrument/measurement noise. However, the noise treatment with the

(51, 3) truncation in the variance analysis is proven useful in detecting weak E_s variances. By removing large spikes from clock errors, the E_s variance maps have showed fewer patchy spots and more consistent patterns between the SNR and phase results.

6. Summary and Future Work

[51] In this paper we described a novel variance analysis on the 50-Hz SNR and phase measurements from satellite radio occultation. The method is applied to GPS/CHAMP data and produces new information on global E_s morphology. The important results are summarized as follows:

[52] 1. The 51-point (or 1-s) variances from CHAMP SNR and phase data reveal strong E_s enhancements at summertime midlatitudes. The maximum E_s variance appears at ~105 km near 45°S in January 2003 and ~102 km near 45°N in June 2002.

[53] 2. The seasonal variation of the E_s variances shows a height-dependent morphology. The variance in the NH midlatitude summer peaks slightly later in time at higher altitudes.

[54] 3. Global E_s variance maps show strong dependence of the E_s strength on the geomagnetic dip angle at 105 km. The summertime midlatitude E_s occurs mostly at $|I| = 30°–60°$, while the wintertime polar E_s exists mainly in the SH within $|I| > 80°$.

[55] 4. CHAMP also observes a strong semidiurnal variation in the midlatitude E_s variances with peak hours around 0800–1000 and 2000 LST at 100 km for the JJA season. The peak hours are delayed as height decreases and the 2000 LST variance maximum extends to a slightly lower height. For the DJF season the summertime E_s enhancement is dominated by a diurnal variation with the peak hour near 2000 LST.

[56] 5. Simulations using a radio wave propagation model suggest that the SNR and phase variances have different characteristics in the "observational filter" for E_s-induced perturbations. The SNR variance has the maximum response at a vertical scale of ~1.2 km, and this characteristic scale is nearly independent of the truncation length used. On the other hand, the characteristic vertical scale of the phase variance increases with the truncation length, varying from 2 km in 51-point truncation to 8 km in 201-point truncation.

[57] The initial results from GPS/CHAMP occultation reveal great potentials for observing global E_s phenomena. We anticipate more exciting results from other existing and upcoming GPS occultation missions, including SAC-C, Gravity Recovery and Climate Experiment, and COSMIC. With the improved global coverage and sampling (~250 occultations/antenna), the seasonal and diurnal variations of E_s can be fully resolved, along with the dependence on geomagnetic field, dynamic wind shear, metastable ions, solar radiation, and particle precipitation. Studies similar to this variance analysis can be readily extended to other GPS occultation measurements, and the joint analysis with the recent wind measurements from Thermosphere, Ionosphere, Mesosphere, Energetics and Dynamics satellite will be very useful for understanding the role of the horizontal winds. Global E_s observations from GPS radio occultation have raised some challenging issues for current E_s theory and models, and reliable statistics of global E_s morphology will add strong constraints on the underlying physical mechanisms in E_s generation and variation.

[58] **Acknowledgments.** We would like to thank Tom Meehan and Byron Iijima for modifying CHAMP operation algorithm that enables the E_s observations at high tangent heights. This research was performed at the Jet Propulsion Laboratory, California Institute of Technology, under contract with the National Aeronautics and Space Administration (NASA). Work done by G. Hajj is supported in part by funding from the National Science Foundation under grant ATM-0210088.

[59] Arthur Richmond thanks Klemens Hocke and Toshitaka Tsuda for their assistance in evaluating this paper.

References

Ao, C. O., et al. (2003), Lower troposphere refractivity bias in GPS occultation retrievals, *J. Geophys. Res.*, *108*(D18), 4577, doi:10.1029/2002JD003216.

Baggaley, W. J. (1984), Ionospheric sporadic-*E* parameters: Longterm trends, *Science*, *225*, 830–831.

Carter, L. N., and J. M. Forbes (1999), Global transport and localized layering of metallic ions in the upper atmosphere, *Ann. Geophys.*, *17*, 190–209.

Coco, D. S., T. L. Gaussiran II, and C. Coker (1995), Passive detection of sporadic *E* using GPS phase measurements, *Radio Sci.*, *30*, 1869–1874.

Datta, R. N. (1972), An interpretation of the global characteristics of thunderstorm effect on sporadic-E ionization, *Indian J. Pure Appl. Phys.*, *10*, 639–640.

Earle, G. D., R. L. Bishop, Q. H. Zhou, and S. P. Wallace (1998), A comparative study of in-situ and remote intermediate layer measurements against wind model predictions of vertical ion drift, *J. Atmos. Sol. Terr. Phys.*, *60*, 1313–1330.

Farley, D. T. (1985), Theory of equatorial electrojet plasma waves: New developments and current status, *J. Atmos. Terr. Phys.*, *47*, 729–744.

Fukao, S., M. Yamamoto, R. T. Tsunoda, H. Hayakawa, and T. Mukai (1998), The SEEK (sporadic-*E* experiment over Kyushu) campaign, *Geophys. Res. Lett.*, *25*, 1761–1764.

Gorbunov, M. E. (2002), Canonical transform method for processing radio occultation data in the lower troposphere, *Radio Sci.*, *37*(5), 1076, doi:10.1029/2000RS002592.

Hajj, G. A., and L. J. Romans (1998), Ionospheric electron density profiles obtained with the Global Positioning System: Results from the GPS/MET experiment, *Radio Sci.*, *33*, 175–190.

Hajj, G. A., et al. (2002), A technical description of atmospheric sounding by GPS occultation, *J. Atmos. Sol. Terr. Phys.*, *64*, 451–469.

Hajj, G. A., C. O. Ao, B. A. Iijima, D. Kuang, E. R. Kursinski, A. J. Mannucci, T. K. Meehan, L. J. Romans, M. de la Torre Juarez, and T. P. Yunck (2004), CHAMP and SAC-C atmospheric occultation results and intercomparisons, *J. Geophys. Res.*, *109*, D06109, doi:10.1029/2003JD003909.

Hocke, K., and T. Tsuda (2001), Gravity waves and ionospheric irregularities over tropical convection zones observed by GPS/MET radio occultation, *Geophys. Res. Lett.*, *28*, 2815–2818.

Hocke, K., et al. (2001), Global sounding of sporadic *E* layers by the GPS/MET radio occultation experiment, *J. Atmos. Sol. Terr. Phys.*, *63*, 1973–1980.

Hocke, K., K. Igarashi, and A. Pavelyev (2002), Irregularities of the topside ionosphere observed by GPS/MET radio occultation, *Radio Sci.*, *37*(6), 1101, doi:10.1029/2001RS002599.

Igarashi, K., A. Pavelyev, J. Wickert, K. Hocke, and D. Pavelyev (2002), Application of radio holographic method for observation of altitude variations of the electron density in the mesosphere/lower thermosphere using GPS/MET radio occultation data, *J. Atmos. Sol. Terr. Phys.*, *64*, 959–969.

Karayel, E. T., and D. P. Hinson (1997), Sub-Fresnel-scale vertical resolution in atmospheric profiles from radio occultation, *Radio Sci.*, *32*, 411–423.

Kelly, M. S. (1989), *The Earth's Ionosphere*, *Int. Geophys. Ser.*, vol. 43, Elsevier, New York.

Kursinski, , et al. (1997), Observing Earth's atmosphere with radio occultation measurements using the Global Positioning System, *J. Geophys. Res.*, *102*, 23,429–23,465.

Levy, M. (2000), *Parabolic Equation Methods for Electromagnetic Wave Propagation*, Inst. of Electr. Eng., London.

Maksyutin, S. V., O. N. Sherstyukov, and A. N. Fahrutdinova (2001), Dependence of sporadic-*E* layer and lower thermosphere dynamics on solar activity, *Adv. Space Res.*, *27*, 1265–1270.

Martin, J. M., and S. M. Flatté (1988), Intensity images and statistics from numerical simulation of wave propagation in 3-D random media, *Appl. Opt.*, *27*(11), 2111–2126.

Mathews, J. D. (1998), Sporadic *E*: Current views and recent progress, *J. Atmos. Sol. Terr. Phys.*, *60*, 413–435.
Mathews, J. D., Y. T. Morton, and Q. Zhou (1993), Observations of ion layer motions during the AIDA campaign, *J. Atmos. Terr. Phys.*, *55*, 447–457.
Pancheva, D., C. Haldoupis, C. E. Meek, A. H. Manson, and N. J. Mitchell (2003), Evidence of a role for modulated atmospheric tides in the dependence of sporadic *E* layers on planetary waves, *J. Geophys. Res.*, *108*(A5), 1176, doi:10.1029/2002JA009788.
Shrestha, K. L. (1971), Sporadic E and atmospheric pressure waves, *J. Atmos. Terr. Phys.*, *33*, 205–206.
Sokolovskiy, S. V. (2001), Modeling and inverting radio occultation signals in the moist troposphere, *Radio Sci.*, *36*, 441–458.
Spilker, J. J. (1980), GPS signal structure and performance characteristics, paper presented at ION GPS Meeting, pp. 29–54, Inst. of Navig., Washington, D. C.
Straus, P. R., P. C. Anderson, and J. E. Danaher (2003), GPS occultation sensor observations of ionospheric scintillation, *Geophys. Res. Lett.*, *30*(8), 1436, doi:10.1029/2002GL016503.
Tsunoda, R. T., and R. B. Cosgrove (2001), Coupled electrodynamics in the nighttime midlatitude ionosphere, *Geophys. Res. Lett.*, *28*, 4171–4174.
Tsunoda, R. T., S. Fukao, and M. Yamamoto (1994), On the origin of quasi-periodic radar backscatter from midlatitude sporadic *E*, *Radio Sci.*, *29*, 349–366.
Ware, R., et al. (1996), GPS sounding of the atmosphere from low Earth orbit: Preliminary results, *Bull. Am. Meteorol. Soc.*, *77*, 19–40.
Whitehead, J. D. (1961), The formation of the Sporadic-*E* layer in the temperate zones, *J. Atmos. Terr. Phys.*, *20*, 49–58.
Whitehead, J. D. (1989), Recent work on mid-latitude and equatorial sporadic *E*, *J. Atmos. Terr. Phys.*, *51*, 401–424.
Wickert, J., et al. (2001), Atmosphere sounding by GPS ratio occultation: First results from CHAMP, *Geophys. Res. Lett.*, *28*, 3263–3266.
Zhang, S. P., et al. (2003), Climatology of neutral winds in the lower thermosphere over Millstone Hill (42.6°N) observed from ground and from space, *J. Geophys. Res.*, *108*(A1), 1051, doi:10.1029/2002JA009512.

C. O. Ao, M. de la Torre Juarez, G. A. Hajj, A. J. Mannucci, and D. L. Wu, Jet Propulsion Laboratory, California Institute of Technology, 4800 Oak Grove Dr., MS 238-600, Pasadena, CA 91109-8099, USA. (dwu@mls.jpl.nasa.gov)